coatings

MDPI

Article

Prediction of Deposition Layer Morphology Dimensions Based on PSO-SVR for Laser–arc Hybrid Additive Manufacturing

Junhua Wang [1,2,3,*], Junfei Xu [1], Yan Lu [4], Tancheng Xie [1,2,3,*], Jianjun Peng [1], Junliang Chen [5] and Yanwei Xu [1]

[1] School of Mechanical and Electrical Engineering, Henan University of Science and Technology, Luoyang 471003, China; mecha_xjf@163.com (J.X.); pjjsdu@163.com (J.P.); xuyanweiluoyang@163.com (Y.X.)
[2] Henan Intelligent Manufacturing Equipment Engineering Technology Research Center, Luoyang 471003, China
[3] Henan Engineering Laboratory of Intelligent Numerical Control Equipment, Luoyang 471003, China
[4] School of Materials Science and Engineering, Henan University of Science and Technology, Luoyang 471023, China; luyan@haust.edu.cn
[5] College of Food and Bioengineering, Henan University of Science and Technology, Luoyang 471023, China; junliangchen@126.com
* Correspondence: wangjh@haust.edu.cn (J.W.); xietc@haust.edu.cn (T.X.)

Abstract: Laser–arc composite additive manufacturing holds significant potential for a wide range of industrial applications, and the control of morphological dimensions in the deposited layer is a critical aspect of this technology. The width and height dimensions within the deposited layer of laser–arc hybrid additive manufacturing serve as essential indicators of its morphological characteristics, directly influencing the shape quality of the deposited layer. Accurate prediction of the shape dimensions becomes crucial in providing effective guidance for size control. To achieve precise prediction of shape dimensions in laser–arc composite additive manufacturing and ensure effective regulation of the deposited layer's shape quality, this study introduces a novel approach that combines a particle swarm algorithm (PSO) with an optimized support vector regression (SVR) technique. By optimizing the SVR parameters through the PSO algorithm, the SVR model is enhanced and fine-tuned to accurately predict the shape dimensions of the deposited layers. In this study, a series of 25 laser–arc hybrid additive manufacturing experiments were conducted to compare different approaches. Specifically, the SVR model was built using selected radial basis function (rbf) kernel functions. Furthermore, the penalty factors and kernel parameters of the SVR model were optimized using the particle swarm optimization (PSO) algorithm, leading to the development of a PSO-SVR prediction model for the morphological dimensions of the deposited layers. The performance of the PSO-SVR model was compared with that of the SVR, BPNN, and LightGBM models. Model accuracy was evaluated using a test set, revealing average relative errors of 2.39%, 7.719%, 9.46%, and 5.356% for the PSO-SVR, SVR, BPNN, and LightGBM models, respectively. The PSO-SVR model exhibited excellent prediction accuracy with minimal fluctuations in prediction error. This performance demonstrates the model's ability to effectively capture the intricate and non-linear relationship between process parameters and deposition layer dimensions. Consequently, the PSO-SVR model can provide a foundation for the control of morphological dimensions in the deposition layer, offering an effective guide for deposition layer morphology dimension control in laser–arc composite additive manufacturing.

Keywords: laser–arc hybrid additive manufacturing; particle swarm optimization; support vector regression

check for updates

Citation: Wang, J.; Xu, J.; Lu, Y.; Xie, T.; Peng, J.; Chen, J.; Xu, Y. Prediction of Deposition Layer Morphology Dimensions Based on PSO-SVR for Laser–arc Hybrid Additive Manufacturing. *Coatings* **2023**, *13*, 1066. https://doi.org/10.3390/coatings13061066

Academic Editor: Michał Kulka

Received: 18 May 2023
Revised: 2 June 2023
Accepted: 6 June 2023
Published: 8 June 2023

Copyright: © 2023 by the authors. Licensee MDPI, Basel, Switzerland. This article is an open access article distributed under the terms and conditions of the Creative Commons Attribution (CC BY) license (https://creativecommons.org/licenses/by/4.0/).

1. Introduction

Laser–arc hybrid additive manufacturing technology amalgamates the dual heat sources of laser melting and arc melting to enable swift formation and customized manufacturing of metallic materials [1]. By harnessing the precise attributes of laser melting

in conjunction with the rapid characteristics of arc melting, this technology emerges as a promising innovation with broad applicability in diverse industrial domains. In comparison to traditional laser or arc additive forming techniques, laser–arc composite additive forming showcases enhanced efficiency and superior processing outcomes [2]. Its advantages, such as expansive formation size, exceptional accuracy, and optimal utilization of raw materials, have propelled its extensive adoption in aerospace, rail transportation, and automotive manufacturing sectors [3]. The width and height of the deposited layer assume crucial roles as fundamental indicators of its dimensional properties. Variations in these dimensions directly impact the quality of the deposited layer. Inadequate width and height not only impede formation efficiency but also exacerbate the risks associated with thermal stress and material deformation. The dimensional attributes of the deposited layer are influenced by multiple factors, including laser power, arc current, and scanning speed. A comprehensive exploration of the intricate mapping relationship between process parameters and deposited layer dimensions can facilitate accurate prediction of the deposited layer's quality under specific parameter settings. This understanding holds paramount significance in regulating deposited layer dimensions, thereby enhancing formation quality and efficiency.

The laser–arc hybrid additive manufacturing has received a lot of attention and research due to its unique advantages. Miaoran Liu et al. [4] prepared thin-walled aluminium alloy parts by arc and laser–arc composite additions, analysed and compared their microstructure and tensile properties, and found that all aspects of the laser–arc composite additions were improved. Zhaodong Zhang et al. [5], in their study of laser-induced MIG arc additive manufacturing of aluminium alloys, explored the effect of laser power on melt pool size by conducting thin-walled part forming tests with different laser powers. Mengcheng Gong et al. [6] investigated the effect of laser power laser–arc composite additive manufacturing of 316L. The results showed that the surface accuracy increases and then decreases with increasing laser power, and the surface hardness decreases with increasing deposition layer height. A large number of studies have made great progress in the mechanisms of laser and arc action, as well as the microstructure and mechanical properties of formed parts. However, relatively little research has been done on the relationship between process parameters and the mapping of deposited layer morphology to size, and on the prediction of deposited layer dimensions.

A common prediction method currently used is to build a finite element model. Chong Wang et al. [7] analysed the thermal behaviour of a composite additive process by developing a three-dimensional steady-state finite element model with two independent surface heat sources, and the predicted melt pool geometry and heat affected zone were in high agreement with the experimental data. However, the utilization of finite element simulation in the context of laser–arc hybrid additive manufacturing encounters inherent limitations. These constraints manifest in the form of an incomplete comprehension of the intricate multi-field coupling process involved in this manufacturing technique, the current uncertainty surrounding the deposition layer change process, and the substantial dependence of finite element accuracy on factors such as cell type, boundary conditions, and mesh scheme. Consequently, the accuracy and stability of predictions derived from finite element modelling are substantially compromised, necessitating further advancements in order to enhance their efficacy. Machine learning methods are widely employed as a prevalent approach for prediction in various fields. Aman Garg et al. [8] used a support vector machine (SVM) algorithm and a Gaussian process regression (GPR) to predict the compressive strength of concrete containing silica nanoparticles. The results showed that SVM can give more accurate prediction results. Aman Garg et al. [9] evaluated the stiffness matrix of functionally graded (FG) nanoplate using a Gaussian process regression (GPR) based surrogate model in the framework of the layerwise theory; the results showed that the method has excellent performance. Compared to finite element methods, machine learning can predict the dynamics of manufacturing processes more quickly and accurately without the need for complex physical knowledge, and it has gained widespread attention and application

in the field of additive manufacturing in recent years [10]. Wang Z et al. [11] used a Particle Swarm Optimisation(PSO) algorithm to optimise the weights and thresholds of the Back-propagation neural network (BPNN) to build a PSO-BP prediction model, and the results showed that the model has high prediction accuracy. Hao J et al. [12] used SVR, PSO-BPNN, and XGBoost models to predict the morphology of the laser cladding layer in the tilted state, and XGBoost showed better prediction performance. Wang K et al. [13] reviewed the application of neural network models, genetic algorithms, and particle swarm algorithms in the optimization of laser cladding process parameters, and analysed and summarized their advantages and disadvantages. The predominant focus of current research resides in laser additive manufacturing or arc additive manufacturing, while comparatively limited attention has been directed towards laser–arc hybrid additive manufacturing. To facilitate the broader implementation of laser–arc hybrid additive manufacturing in industrial settings, this study employs machine learning methodologies to forecast the morphological dimensions of deposited layers in laser–arc composite additive manufacturing. The outcome of this research serves as a crucial foundation for regulating the deposited layers and selecting optimal process parameters. Given the inherent nature of laser–arc hybrid additive manufacturing as a predominantly small sample experiment, the widely employed Backpropagation neural network (BPNN) algorithm is found to be inadequate due to its susceptibility to overfitting when confronted with limited sample data [14]. Conversely, the Support Vector Regression (SVR) algorithm demonstrates enhanced stability, robustness, and generalization capabilities for small sample low-dimensional problems [15]. Hence, the SVR algorithm emerges as a more suitable choice for accurate predictions in laser–arc composite additive manufacturing. Nevertheless, it is worth noting that the prediction accuracy of SVR models can be substantially influenced by penalty factors, kernel parameters, and other related factors. Conventional approaches relying on manually pre-set parameters often yield unsatisfactory prediction outcomes. To address this limitation, the current study leverages a particle swarm optimization algorithm characterized by superior global search capabilities. This optimization technique is employed to fine-tune the parameters of the SVR model, thereby enhancing the prediction accuracy of the model significantly.

This study introduces a novel approach by combining the Particle Swarm Optimization (PSO) algorithm with the Support Vector Regression (SVR) algorithm to develop a PSO-SVR-based prediction model for sediment layer topography. Experimental results were employed to construct a support vector regression model for the process parameters and deposition layer topography size. The PSO algorithm was then utilized to optimize the penalty factor and kernel parameters of the SVR algorithm, resulting in a highly accurate PSO-SVR prediction model. The performance of the PSO-SVR model was compared with that of BPNN, SVR, and Light Gradient Boosting Machine (LightGBM) models to assess its prediction accuracy. The findings of this study provide valuable insights for effective control of the form size, serving as a decision-making reference and guidance for enhancing both the quality and efficiency of the forming process.

2. Materials and Methods

2.1. Materials and Setup

All experiments in this study were carried out on a laser–arc hybrid additive manufacturing system. The schematic diagram of the aforementioned system is presented in Figure 1. The system consisted of an electric arc unit, a laser, and a cooling system. Specifically, an electric arc unit powered by a Kaierda D350S was employed, while the laser beam was generated by an RFL-2000W laser. In the course of the experimentation, the displacement of the laser and arc units was carried out by a Yaskawa GP25 six-axis robot. The protective gas utilized in the experiment was composed of a precise mixture of argon and carbon dioxide, with a consistent flow rate of 6 L/min. In order to mitigate the risk of overheating of the laser head, it is imperative to establish a mechanism for cooling. To this end, the laser head was connected to a water cooler.

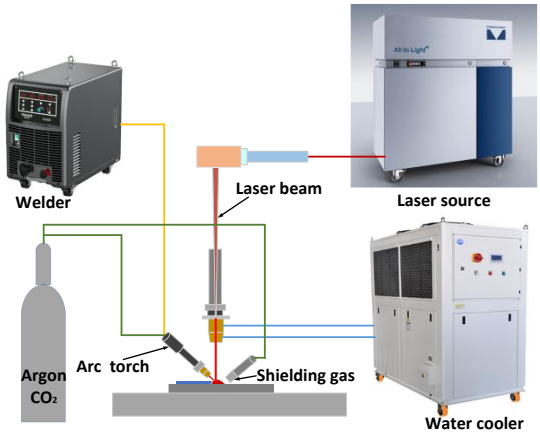


Figure 1. Schematic diagram of the laser–arc hybrid additive manufacturing system.

In this study, the experimental material consisted of substrates made of 45 steel, which were of uniform dimensions measuring 20 × 10 × 8 mm. To minimize any potential impact on the experimental results from external factors, such as heat build-up resulting from repeated processing, each substrate was subjected to a single experiment. Before conducting the experiment, the substrate surface was subjected to abrasion using sandpaper, followed by thorough cleansing to eliminate surface impurities using anhydrous ethanol. This study employed the use of THQ-50C wire as the deposition material, a carbon steel wire of 500 MPa grade, which has been manufactured using advanced drawing and surface copper plating processes. This material is favoured for its superior properties, which include low spatter, high deposition efficiency, excellent deposition layer formation, and low metal porosity sensitivity. Due to these exceptional features, THQ-50C wire finds widespread application in construction machinery, ships, and petrochemical industries. In this study, a wire with a diameter of 0.8 mm was utilized, and Table 1 displays the chemical composition of THQ-50C.

Table 1. Chemical composition of THQ-50C.

Element	C	Mn	Si	S	P	Cr	Ni	Cu	Mo	V
Wt%	0.08	1.50	0.89	0.012	0.013	0.02	0.03	0.11	0.002	0.003

2.2. Design of Experiments

The use of the orthogonal test method provides a significant advantage in obtaining sample data that is evenly distributed. Furthermore, this approach meets the demands of test design by reducing the number of experiments required, leading to improved testing efficiency and cost-effectiveness. The primary objective of the present study was to establish a predictive model elucidating the relationship between process parameters and the morphology dimensions of the deposited layer. To accomplish this objective, welding current, laser power, and scanning speed were selected as input variables, while the output variables comprised the width and height of the deposited layer. Employing the orthogonal test method, a meticulous construction of 25 sets of three-factor five-level orthogonal tests was conducted. Each factor, namely welding current, laser power, and scanning speed, was assigned five levels. Table 2 shows the details about the design of experiments.

Table 2. Design of experiments.

Process Parameters (Symbol, Unit)	Value
Laser power (P, W)	500, 600, 700, 800, 900
Scan speed (v, mm/s)	6, 8, 10, 12, 14
Welding current (I, A)	80, 100, 120, 140, 160
Argon gas flux (Q, L/min)	6
Laser spot diameter (d, mm)	3

3. Results

A total of twenty-five sets of Laser–arc hybrid additive manufacturing experiments were conducted in this study, employing diverse process parameters as outlined in Table 2. To analyse the deposited layer, a wire cutter was employed to section it perpendicular to the scanning direction. The resulting cross-sectional samples underwent a series of sanding and polishing procedures, utilizing increasingly finer sandpapers, including #200, #400, #600, #800, #1000, #1500, #1800, and #2200. Following this, a grinding and polishing machine was used to further refine the samples, which were subsequently subjected to etching using a 5% nitric acid alcohol solution. Finally, the cross-sectional morphology of the deposited layer was visualized under an optical microscope, and the resultant image is presented in Figure 2.

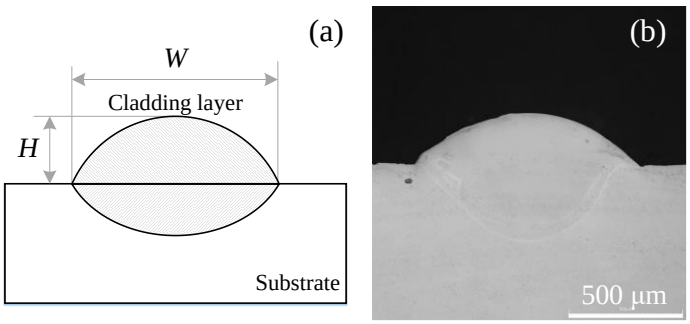


Figure 2. Cross section of deposition layer. (**a**) The schematic diagram; (**b**) the sample.

The width and height of the deposited layer were measured using ImageJ software to obtain the width and height of the deposited layer for different process parameters, and the results of the orthogonal tests are shown in Table 3. P, V, and A in the table represent the three process parameters of laser power, scanning speed and welding current, respectively; W and H represent the width and height of the deposited layer, respectively.

Table 3. Orthogonal experiment results.

NO.	P/(W)	V/(mm·s^{-1})	I/(A)	W/mm	H/mm
1	800	14	140	4.952	1.482
2	700	12	80	4.714	0.917
3	700	14	160	5.467	1.405
4	700	8	120	5.881	1.751
5	700	6	140	7.018	2.431
6	900	14	120	5.065	1.294
7	500	10	140	5.446	1.631
8	800	8	100	5.417	1.417
9	800	6	120	6.411	2.192
10	500	12	120	5.155	1.369
11	900	10	160	6.827	1.932
12	800	12	160	6.583	1.840
13	600	8	140	6.208	2.111
14	600	12	100	4887	1.095
15	900	6	100	5.976	1.792
16	600	10	120	5.351	1.421
17	900	12	140	5.583	1.528
18	500	6	80	5.381	1.508
19	500	8	160	7.537	2.302
20	500	14	100	4.789	1.004
21	700	10	100	5.143	1.191
22	900	8	80	5.272	1.119
23	600	14	80	4.667	0.825
24	600	6	160	8.506	2.790
25	800	10	80	4.801	1.059

In this study, we sought to investigate the influence of different process parameters on the width and height of the deposited layer in laser–arc compounding processes. To this end, we conducted an analysis of variance (ANOVA) on the experimental results to identify the key factors affecting the deposition layer width. Our findings revealed that the laser–arc compounding process parameters have varying degrees of impact on the deposited layer width. Specifically, the arc current exerted the most significant influence, followed by the scanning speed, whereas the laser power had the least effect. To gain a deeper understanding of the relationship between the process parameters and the deposition layer width, we performed a multivariate nonlinear fit using the nonlinear least squares Marquardt method. In this analysis, the process parameters were treated as independent variables, while the deposition layer width was considered as the dependent variable. A total of 25 sets of experiments were conducted to obtain the objective function, which characterizes the relationship between the process parameters and the deposition layer width. The objective function obtained from the analysis is presented below:

$$W = 1.408\left(P^{0.013} \times I^{0.425} \times V^{-0.319}\right) + 1.452 \quad (1)$$

The analysis of the objective function derived from the multivariate nonlinear fit revealed notable relationships between the deposition layer width and various process parameters. Specifically, the width was found to exhibit a positive correlation with arc current, while an inverse correlation was observed with scan speed. On the other hand, the laser power was determined to have a negligible impact on the deposited layer height. The investigation demonstrated that increasing the arc current led to an increase in the deposition layer width, whereas an escalation in the scan speed resulted in a decrease in the width. It is important to note that the influence of these parameters on the deposition layer width is not equal, with arc current exerting a more pronounced effect compared to scan speed.

A similar analysis was conducted to examine the impact of the laser–arc composite process parameters on the deposition layer height. Specifically, an ANOVA was performed on the deposition layer height, and the results indicated that the arc current had the most significant influence on the deposition layer height, followed by the scanning speed, while the laser power had the least effect. Subsequently, a multivariate non-linear fit was carried out on the experimental results using the non-linear least squares Marquardt method. This analysis aimed to obtain the objective function of the deposition layer height and the laser melting process parameters, with the process parameters as the independent variables and the deposition layer height as the dependent variable. The obtained objective function is presented below:

$$H = 0.713\left(P^{0.016} \times I^{0.938} \times V^{-0.675}\right) - 0.194 \quad (2)$$

The analysis of the objective function demonstrates that the height of the deposited layer increases with the increase in the arc current, whereas it decreases with the increase in the scanning speed. Furthermore, it was found that the laser power does not have a significant impact on the deposited layer height.

The analysis reveals that an increase in arc current leads to a subsequent increase in arc pressure. This elevated arc pressure exerts a greater force on the liquid melt pool, consequently expanding the cross-sectional area of the pool. Consequently, both the layer width and layer height of the monolayer experience an increase. Conversely, when parameters such as arc current remain constant, an increase in scanning speed results in a reduction in the amount of molten metal per unit time and a decrease in heat input. This reduction in heat input, coupled with the decreased amount of molten metal, subsequently causes a decrease in both the width and height of the deposited layer as the scanning speed increases.

4. Prediction Modelling

4.1. Support Vector Regression Model

The morphological dimensions of laser–arc hybrid additive manufacturing deposited layers are subject to the influence of several factors, with process parameter variations directly impacting the deposited layer morphological dimensions. The relationship between process parameters and deposited layer dimensions is non-linear, rendering traditional methods ineffective in establishing correlations between process parameters and deposited layer dimensions and in accurately predicting the deposited layer. Support Vector Regression (SVR) is a machine learning method that relies on statistical theory and minimization of structural risk principles [16]. This method demonstrates outstanding performance in resolving small sample high-dimensional non-linear problems by constructing non-linear mapping relationships between input and output variables in an efficient and precise manner [17]. Therefore, SVR is an ideal method for solving the problem of predicting the size of deposition layers in laser–arc hybrid additive manufacturing. The structure of the SVR is shown in Figure 3.

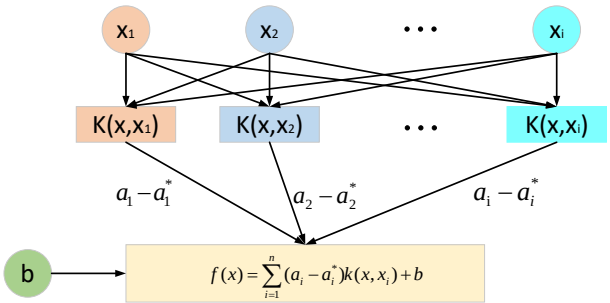


Figure 3. Schematic diagram of the SVR structure.

The present study aims to predict the size of the deposition layer in laser–arc hybrid additive manufacturing using support vector regression. To this end, the support vector regression problem can be formulated as follows: given the experimental results of laser–arc hybrid additive manufacturing, it is hypothesized that there exists a functional relationship between the target prediction f(x) and the input x. This functional relationship can be mathematically expressed as a function of x. The functional form can be expressed as follows:

$$\mathrm{f}(x) = \omega^T \varphi(x) + b \tag{3}$$

where $\varphi(x)$ is the nonlinear mapping function; ω^T is the weight vector; x is the input vector; $x = \{x_1, x_2, \cdots, x_i\}$ represents different process parameters; and b is the bias term.

In accordance with the principle of structural risk minimization, the regression problem for the aforementioned function can be addressed by solving the parameters ω and b via the minimization of the structural risk R_{str} [18].

$$\min R_{st} = \frac{1}{2}(\omega \cdot \omega) + \frac{c}{l}\sum_{i=1}^{l}|f(x_i) - y_i|_\varepsilon \tag{4}$$

c indicates the penalty factor; ε is the insensitive loss function, defined as:

$$|f(x_i) - y_i|_\varepsilon = \begin{cases} |f(x_i) - y_i| - \varepsilon & |f(x_i) - y_i| \geq \varepsilon \\ 0 & |f(x_i) - y_i| < \varepsilon \end{cases} \tag{5}$$

With the introduction of slack variables ξ_i and ξ_i^*, the above equation can be transformed into an equivalent optimization problem.

$$\min \frac{1}{2}\|\omega\|^2 + c\sum_{i=1}^{l}(\xi_i + \xi_i^*) \tag{6}$$

$$\text{S.t.} \qquad y_i - \left[\omega^T \varphi(x_i) + b\right] \leq \varepsilon + \xi_i$$

$$\left[\omega^T \varphi(x_i) + b\right] - y_i \leq \varepsilon + \xi_i$$

$$\xi_i, \xi_i^* \geq 0, i = 1, 2, \cdots n \tag{7}$$

By introducing Equation (7) into the Lagrangian function, the kernel function $K(x, x_i)$ of the composite Mercer condition is introduced according to the Karush–Kuhn–Tucker (KKT) condition, and the final regression function obtained can be expressed as:

$$f(x) = \sum_{i=1}^{n} (a_i - a_i^*) k(x, x_i) + b \tag{8}$$

where a_i and a_i^* are Lagrangian multipliers, and b is the bias term.

The kernel function is an indispensable parameter in Stochastic Vector Regression (SVR) that regulates the non-linear characteristics of the model. The selection of different kernel functions can significantly impact the accuracy of prediction results, as it determines the model's ability to capture complex patterns in the data, which is critical to achieving high predictive performance. This study compares the prediction accuracy of the linear kernel function, the poly (polynomial function) kernel function, the rbf (Gaussian radial basis) kernel function, and the sigmoid kernel function, to identify the optimal kernel function for model construction.

(1) The poly kernel function formula:

$$k(x, x_i) = \left(x^T x_i\right)^d \tag{9}$$

(2) The rbf kernel function formula:

$$k(x, x_i) = \exp\left(-\frac{\|x - x_i\|^2}{2\sigma^2}\right) \tag{10}$$

(3) The sigmoid kernel function formula:

$$k(x, x_i) = \tanh\left(a x^T x_i + c\right) \tag{11}$$

where tanh is hyperbolic tangent function, $a > 0$, $c > 0$.

(4) The linear kernel function formula:

$$k(x, x_i) = x^T x_i \tag{12}$$

The morphological dimensions of the deposited layer in laser–arc hybrid additive manufacturing is subject to various process parameters, among which laser power, scanning speed, and arc current are considered the most critical factors. These parameters play a significant role in determining the energy input, rate of material deposition, and the extent of material melting and solidification, thereby profoundly influencing the performance of the deposition process. To comprehensively investigate the impact of these key process parameters on the morphological dimensions of the deposited layer in laser–arc composite additive deposition, the present study focuses on the analysis of the deposition layer width and height as output parameters. Additionally, laser power, scanning speed, and arc current are considered as input variables to develop a SVR-based model for accurately predicting the size of the deposition layer.

From the 25 sets of test data, 5 sets were randomly selected as the test set, and the remaining 20 sets were used as the training set for model development and optimization. The experimental data must be normalised to convert all data between [0, 1], which can

hasten convergence and increase prediction accuracy because the magnitudes of the experimental data are not uniform and the values of the various parameters range significantly from one another. The normalized formula is shown as following:

$$X' = \frac{X - X_{\min}}{X_{\max} - X_{\min}} \tag{13}$$

X is the raw data; $X_{\max}$ and $X_{\min}$ are the maximum and minimum values in the raw data, respectively; and X' is the normalised number.

The SVR model was tested using a test dataset after being trained using normalised training data. The prediction accuracy of the model was assessed by contrasting the predicted values of the test data with the actual values.

4.2. PSO-SVR Model

The penalty factor, denoted as "c", and the kernel parameter, denoted as "g", constitute crucial components of the support vector regression (SVR) model, and their proper selection significantly impacts the model's prediction accuracy. Traditionally, researchers have employed a grid search method to determine the optimal values for c and g. However, this method is exhaustive, time-consuming, and prone to human intervention, which can undermine the accuracy and efficiency of the model. In contrast, Particle Swarm Optimization (PSO) algorithm is a widely-used technique for hyperparameter optimization in machine learning models [19]. The PSO algorithm exhibits strong global search capability, fast convergence, and requires no preprocessing of initial values, which makes it an ideal tool for hyperparameter optimization of SVR models. In this study, a novel approach is proposed for determining the optimal kernel parameter g and penalty factor c for the SVR model, leveraging the PSO algorithm. By employing the PSO algorithm's search capabilities to identify the ideal values of c and g, the SVR model's generalization capability and prediction accuracy are enhanced. As a result, more reliable and accurate predictions can be achieved.

4.2.1. PSO Algorithm

The PSO algorithm is an intelligent optimisation algorithm that simulates the predatory behaviour of birds. The algorithm interprets each individual in the population as a particle in the search space, characterized by its position, velocity, and fitness value [20]. The position of a particle corresponds to a possible solution to the optimization problem, and its fitness value indicates its quality in comparison to other particles. The particles in the population continuously update their position and velocity by monitoring their own local and global optimums (P_{best} and G_{best}). This process is repeated until a stopping criterion is met, such as a maximum number of iterations or a satisfactory level of fitness [21]. The process of updating the velocity and position of the particle is shown in Figure 4, and the formulae are shown in Equations (14) and (15) [22].

$$v_{sd}^{k+1} = \rho v_{sd}^{k} + c_1 r_1 \left(P_{best\ sd} - x_{sd}^{k} \right) + c_2 r_2 \left(G_{best\ sd} - x_{sd}^{k} \right) \tag{14}$$

$$x_{sd}^{k+1} = x_{sd}^{k} + v_{sd}^{k} \tag{15}$$

where $d \in [1, D]$, D indicates the population size; $k \in [1, K]$, K indicates the iteration times; $s \in [1, S]$, S denotes the dimension of the particle; v_{sd}^{k+1} denotes the flight speed of the particle at the k+1st iteration; x_{sd}^{k+1} denotes the position of the particle at the k+1st iteration; $c_1, c_2 \in [1, 2]$ represent the learning factor for individuals and populations, respectively; ρ is the inertia weight; and $r_1, r_2 \in [0, 1]$ is the random constant.

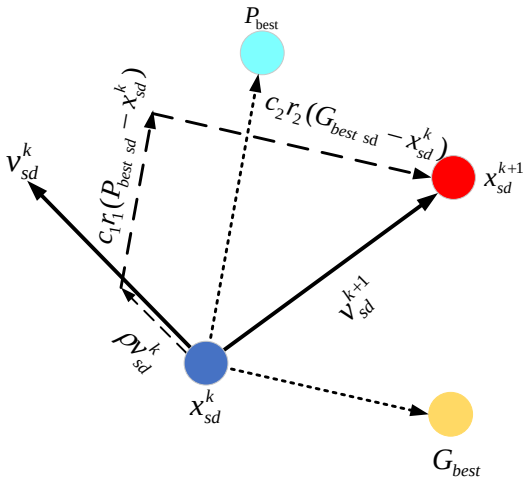


Figure 4. Diagram of the particle renewal process.

4.2.2. PSO-SVR

The present study aims to enhance the predicting accuracy of the SVR model by employing the PSO algorithm to determine the optimal kernel function g and penalty factor c, and thereafter obtain optimal hyperparameters for the SVR model by PSO and use the optimised network to predict sediment layer width and height. The algorithm flow is shown in Figure 5, with the following main steps:

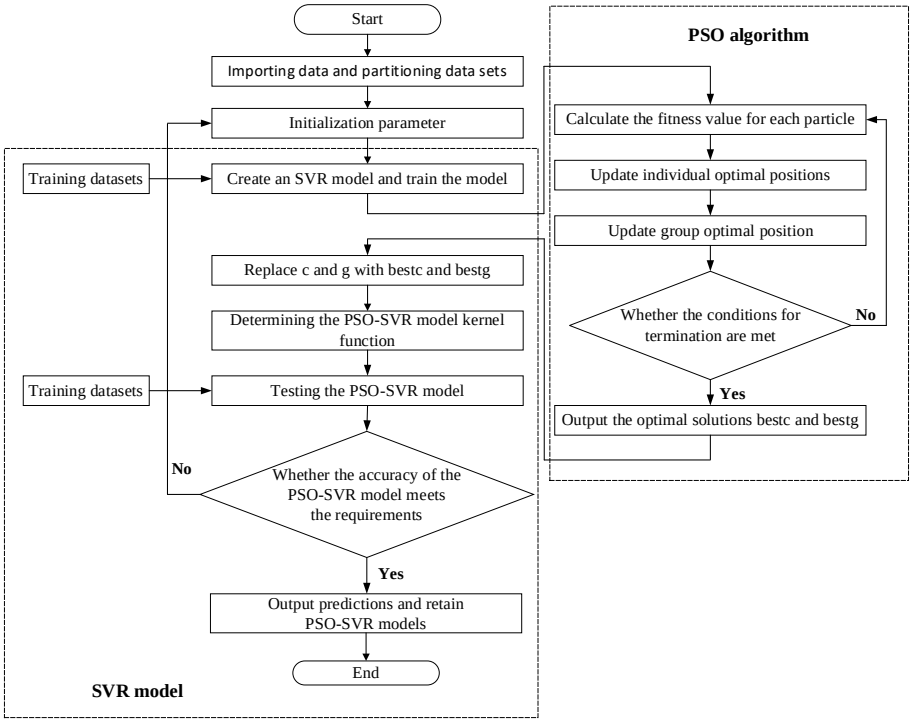


Figure 5. PSO-SVR based laser–arc hybrid additive manufacturing deposition layer morphology size prediction flow chart.

Step 1: Import the deposition layer width and height into the model as output data and the process parameters as input data, dividing the training set and test set.

Step 2: Set the initial parameters, including the number of iterations, the number of populations, the learning factor, the inertia weight, the search range of the kernel parameter g and penalty factor c, and generate a random set of particle velocities and positions.

Step 3: Choose different kernel functions, build the SVR model and train the model using the training set.

Step 4: The outcome of each particle's search is substituted into the SVR model, the mean square error of the anticipated and experimental values acquired from the training process of several SVR models is utilised as the fitness function of the PSO algorithm, and the fitness of all particles is determined.

Step 5: The adaptation for each particle is compared to the adaptation for Pbest, and if the former is superior, the latter is substituted with the particle's present position.

Step 6: As in step 5, update Gbest.

Step 7: Determine to confirm if the termination requirement has been met. The ideal penalty factor bestc and the optimal kernel parameter bestg are output if it is satisfied; otherwise, move on to step 5.

Step 8: Replace c and g in the SVR model with bestc and bestg.

Step 9: Compare the prediction accuracy of the PSO-SVR model with the four common kernel functions and select the kernel function with the highest accuracy to build the PSO-SVR model.

Step 10: Test the PSO-SVR model with the test dataset.

5. Results and Discussion

5.1. Determination of the PSO-SVR Prediction Model Kernel Function

The selection of the kernel function has a considerable impact on the accuracy of prediction results. In this research, four kernel functions, namely the line kernel function, rbf kernel function, sigmoid kernel function, and poly kernel function, are employed to develop PSO-SVR models for predicting the morphological dimensions of deposited layers. A training dataset consisting of twenty sets of experimental data was chosen, and these models were trained using this dataset to assess their respective prediction accuracy. Subsequently, the model with the highest accuracy was selected as the prediction model. To ensure a scientific and objective assessment of the model's prediction performance, this paper utilizes Mean Relative Error (MRE), Mean Square Error (MSE), and Coefficient of Determination (R2) as evaluation metrics to quantitatively evaluate the prediction performance. The specific formula is as follows:

$$R^2 = \frac{\sum_{i=1}^{n} (\hat{y}_i - \overline{y})^2}{\sum_{i=1}^{n} (y_i - \overline{y})^2} \tag{16}$$

$$MSE = \frac{1}{n} \sum_{i=1}^{n} (\hat{y}_i - y_i)^2 \tag{17}$$

$$MRE = \frac{1}{n} \frac{\sum_{i=1}^{n} |\hat{y}_i - y_i|}{y_i} \tag{18}$$

where $\hat{y}_i$ represents the i-th predicted value of the test set; y_i denotes the i-th true value of the test set; and $\overline{y}$ represents the average of the true values of the test data set.

Figure 6 illustrates a comparative analysis between the predicted values and actual values of deposition layer widths for various kernel functions. Specifically, Figure 6a depicts the numerical comparison utilizing the linear kernel function, Figure 6b represents the numerical comparison employing the rbf kernel function, Figure 6c illustrates the numerical comparison using the sigmoid kernel function, and Figure 6d presents the numerical comparison utilizing the poly kernel function.

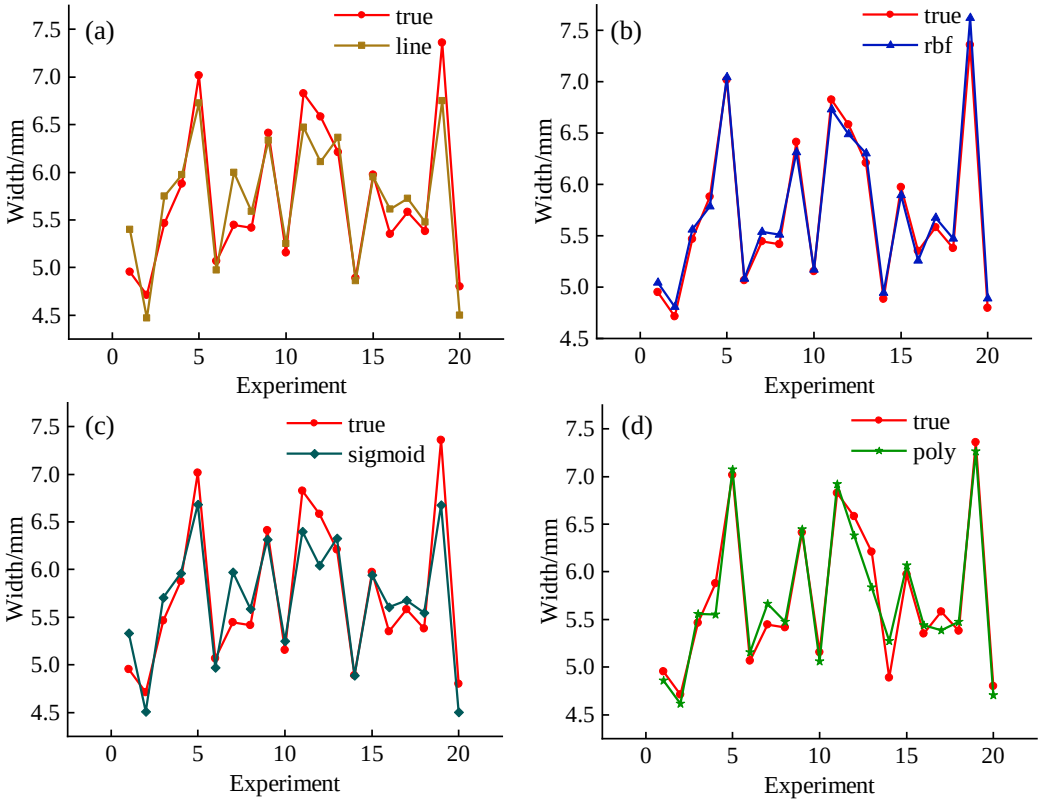


Figure 6. Comparison of predicted and actual values deposition layer widths for different kernel functions. (**a**) Linear kernel function; (**b**) rbf kernel function; (**c**) sigmoid kernel function; (**d**) poly kernel function.

Observing Figure 6, it becomes evident that the predictions generated by the linear kernel function and the sigmoid kernel function exhibit relatively close proximity. However, some deviations persist between the predicted values of these two kernel functions and their corresponding actual values. Conversely, the predictions obtained using the poly kernel function demonstrate fewer deviations from the actual values, although significant deviations are still noticeable in regions characterized by data fluctuations. Among the four kernel functions examined, the rbf kernel function showcases the highest degree of overlap between the predicted and actual values, thereby yielding the highest prediction accuracy. In order to make a more objective comparison of the prediction results, the prediction accuracy of the four kernel functions was calculated, and the results are shown in Table 4.

Table 4. Prediction accuracy indicators for PSO-SVR models with different nuclear parameters.

	Linear	**Rbf**	**Sigmoid**	**Poly**
R^2	0.819	0.992	0.794	0.964
MSE	0.157	0.007	0.179	0.031
MRE	0.048	0.049	0.049	0.025

Table 4 shows that rbf has the minimum MSE and MRE as well as an R^2 that is closest to 1. The results show that the prediction accuracy is highest and the actual values fit the expected values the best when the rbf kernel function is selected.

Four kernel functions were used to forecast the heights of the sediment layers, and Figure 7 compares the predicted and observed values of the deposition layer height for each kernel function.

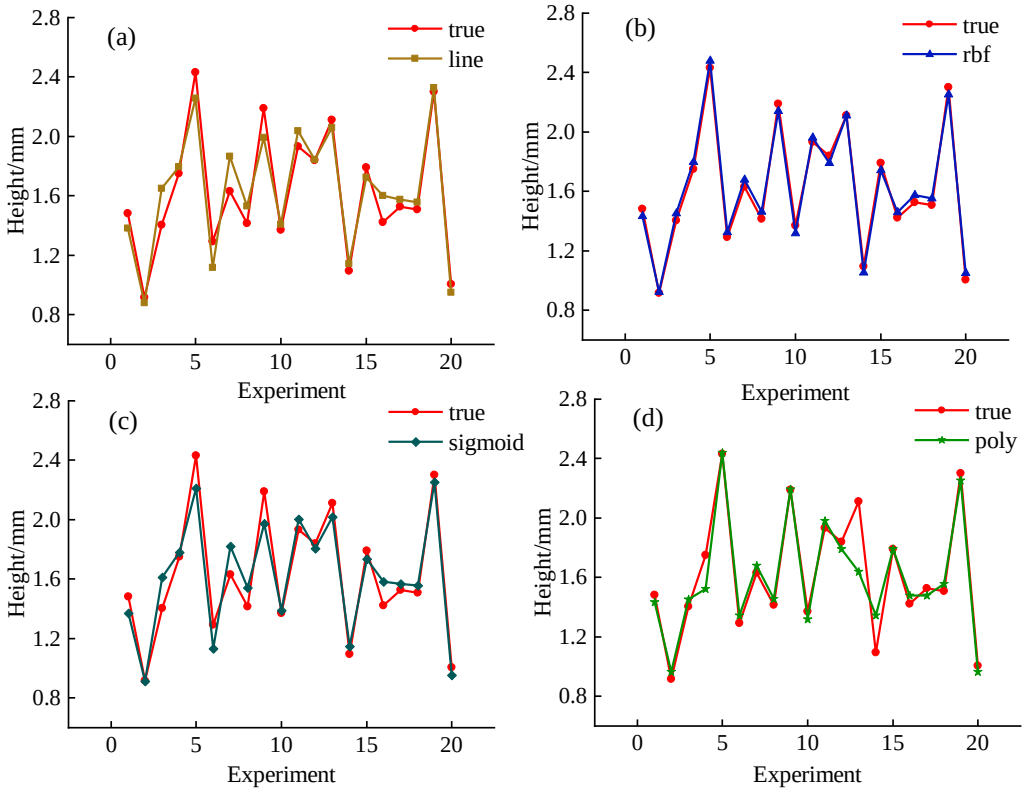


Figure 7. Comparison of predicted and actual values deposition layer height for different kernel functions. (**a**) Linear kernel function; (**b**) rbf kernel function; (**c**) sigmoid kernel function; (**d**) poly kernel function.

The prediction accuracy of the PSO-SVR model was calculated for four different kernel functions and the results are shown in Table 5.

Table 5. Prediction accuracy indicators for PSO-SVR models with different nuclear parameters.

	Linear	**Rbf**	**Sigmoid**	**Poly**
R^2	0.927	0.991	0.905	0.925
MSE	0.017	0.002	0.023	0.018
MRE	0.068	0.027	0.079	0.053

By amalgamating Figures 6 and 7, and Tables 4 and 5, it becomes evident that the utilization of the sigmoid kernel function results in the PSO-SVR model exhibiting the poorest fitting ability and the lowest prediction accuracy. Conversely, when the rbf kernel function is employed, the model showcases the most robust fitting capacity by closely aligning the predicted values with the actual values, thereby yielding higher prediction accuracy. In summary, the rbf kernel function was chosen to construct the PSO-SVR sediment layer size prediction model.

5.2. Comparison of Prediction Results of Different Models

In this study, the PSO-SVR sediment layer size prediction model was built using the rbf kernel function. The predictions utilising the SVR model, BPNN model, LightGBM model, and PSO-SVR model, respectively, were compared in order to further confirm the veracity and accuracy of the PSO-SVR prediction model. In order to demonstrate the prediction

accuracy of each model more visually, the relative error between the predicted and actual values of each model was calculated. The relative error Δ is defined as:

$$\Delta = \left| \frac{X - X'}{X} \right| \times 100\% \tag{19}$$

where X is the actual data value of the test set and X' is the predicted value of the model.

Table 5 presents a comparative analysis of the deposition layer widths between the actual observations and the predictions from various model test sets. In this table, the actual sediment layer width is denoted as W, while the predicted widths from different models, namely PSO-SVR (W1), SVR (W2), BPNN (W3), and LightGBM (W4), are represented accordingly. Moreover, the relative error values for each model's predictions in relation to the actual PSO-SVR values (Δ1), SVR model (Δ2), BPNN model (Δ3), and LightGBM model (Δ4) are also depicted in the table.

A comparison of the prediction results for each model is shown in Figure 8.

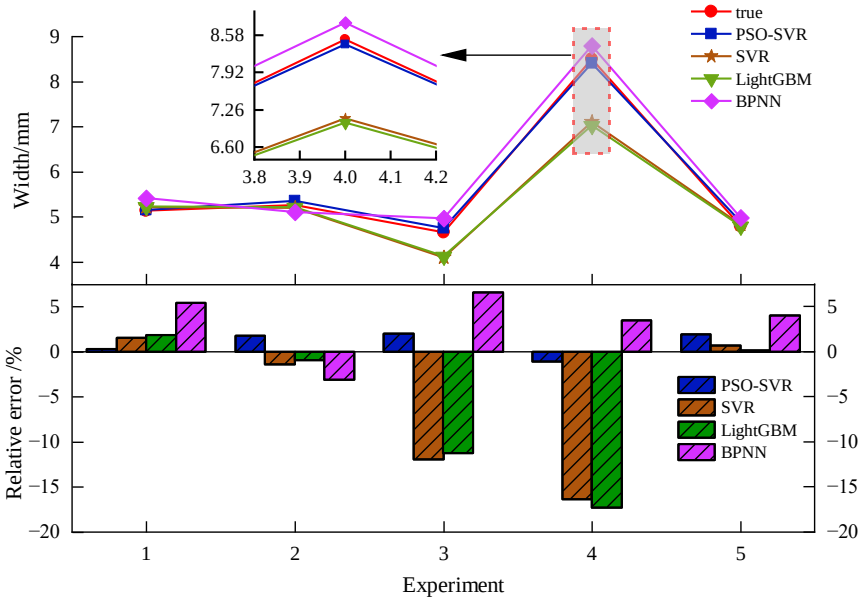


Figure 8. Comparison of predicted sediment layer widths between models.

By integrating the information presented in Table 6 and Figure 8, it becomes evident that the predicted values obtained from the PSO-SVR model exhibit a high degree of concordance with the actual values. Notably, the maximum relative error observed for the PSO-SVR model stands at a mere 1.99%. In contrast, the maximum prediction errors for the SVR model, LightGBM model, and BPNN model are recorded at −16.37%, −17.31%, and 6.57%, respectively. These findings demonstrate that the PSO-SVR model showcases superior predictive accuracy compared to the other models. Moreover, it is worth noting that the PSO-SVR model exhibits lower volatility and greater stability in its prediction errors.

Table 6. Comparison of actual and predicted deposition layer widths for each model test set.

NO.	W	W1	W2	W3	W4	Δ1/%	Δ2/%	Δ3/%	Δ4/%
1	5.143	5.158	5.223	5.236	5.442	0.29	1.55	1.81	5.42
2	5.272	5.355	5.198	5.221	5.221	1.76	−1.43	−0.97	−3.09
3	4.666	4.729	4.109	4.141	4.141	1.99	−11.93	−11.25	6.57
4	8.506	5.413	7.113	7.034	7.034	−1.09	−16.37	−17.31	3.44
5	4.081	4.893	4.835	4.807	4.807	1.91	0.71	0.12	4.04

A comparison of actual and predicted values of sediment layer heights for each model test set is shown in Table 6, where H represents actual values of sediment layer heights,

and H1, H2, H3, and H4 represent predicted values of PSO-SVR heights, predicted values of SVR model, predicted values of BPNN model, and predicted values of LightGBM model, respectively. Δ5, Δ6, Δ7, and Δ8 represent relative errors of predicted and actual values of PSO-SVR, SVR model relative error, BPNN model relative error, and LightGBM model relative error, respectively.

The predicted results of each model are shown in Figure 9.

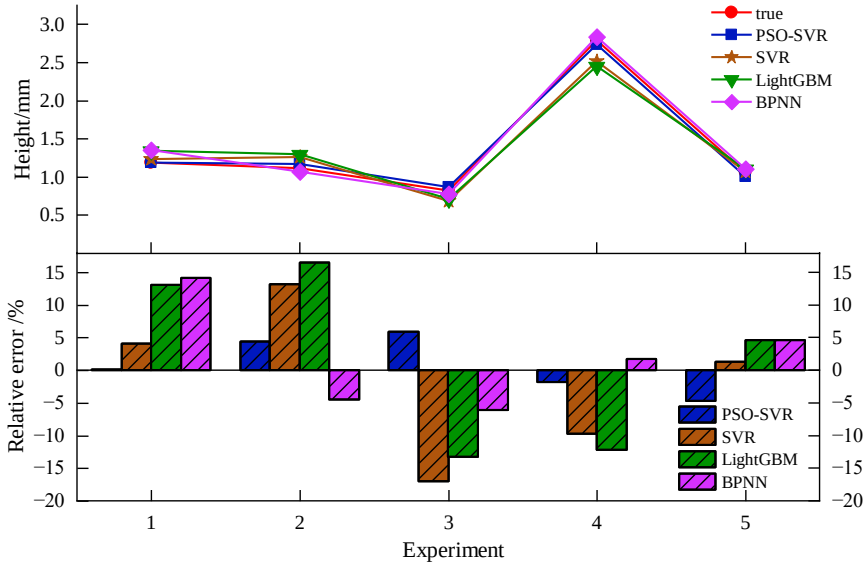


Figure 9. Comparison of predicted sediment layer height between different models.

Combining Figure 9 and Table 7, it can be seen that the maximum relative error of the PSO-SVR model is 5.93%, which is lower than the maximum relative errors of several other models, and the PSO-SVR has the smallest fluctuation in prediction error and the highest prediction accuracy.

Table 7. Comparison of actual and predicted deposition layer height for each model test set.

NO.	H	H1	H2	H3	H4	Δ5/%	Δ6/%	Δ7/%	Δ8/%
1	1.190	1.192	1.238	1.345	1.358	0.16	4.03	13.05	14.11
2	1.119	1.168	1.267	1.304	1.069	4.37	13.22	16.53	−4.46
3	0.825	0.874	0.685	0.716	0.775	5.93	−16.96	−13.21	−6.06
4	2.791	2.741	2.521	2.449	2.839	−1.75	−9.67	−12.22	1.75
5	1.059	1.009	1.073	1.108	1.106	−4.72	1.32	4.62	4.62

To summarize, the PSO-SVR prediction model, employing the rbf kernel function, outperforms other prediction models in all assessed metrics. It consistently exhibits smaller and more stable relative error values, thus enabling a more precise depiction of the non-linear correlation between process parameters and the dimensions of the deposition layer. The heightened prediction accuracy of the PSO-SVR model results in more reliable forecasts of the deposition layer size, carrying significant implications for guiding subsequent analyses and decision-making processes

6. Conclusions

To accurately predict the size of the deposition layer in laser–arc hybrid additive manufacturing, this study proposes the construction of a PSO-SVR-based prediction model. The BPNN, LightGBM, and SVR models were utilized as control models for comparison. A total of 25 sets of experiments were conducted for training and validating the model. Based on the experimental results, the PSO-SVR, SVR, BPNN, and LightGBM models were developed, utilizing laser power, scanning speed, and arc current as input variables, and

deposition layer width and height as output variables, respectively. The average relative error was found to be 2.39% for the PSO-SVR model, 7.719% for the SVR model, 9.46% for the BPNN model, and 5.356% for the LightGBM model. The findings indicate that the PSO-SVR model consistently outperforms the SVR, BPNN, and LightGBM models across all evaluation metrics, demonstrating superior prediction performance. The PSO-SVR model enables more accurate prediction of the deposition layer size in laser–arc composite additive manufacturing. The reliability and accuracy of the PSO-SVR model's predictions have laid a solid foundation for effective control and regulation of the deposition layer morphology in laser–arc composite additive manufacturing.

This study focuses on the prediction of the topography dimensions of laser–arc hybrid additive manufacturing deposited layers. Accurately predicting the morphology dimensions of deposited layers can offer valuable insights for selecting appropriate process parameters, thereby enhancing process quality and minimizing costs. Nevertheless, it is essential to further model and predict other critical performance indicators of the deposited layers, such as tensile strength, hardness, and fatigue properties. These additional predictions will contribute to advancing the application of laser–arc composite additive techniques. Future research endeavours should encompass the integration of more advanced machine learning algorithms and hyperparameter optimization techniques, in conjunction with the algorithms mentioned above, to enhance prediction accuracy. Moreover, there is a necessity to employ such methods to model and predict additional performance metrics associated with the deposited layers.

Author Contributions: Conceptualization, J.W. and J.X.; methodology, J.W. and J.X.; validation, J.W., J.X. and Y.L.; formal analysis, J.X.; investigation, Y.L. and J.C.; resources, J.W.; data curation, Y.L. and J.P.; writing—original draft preparation, J.X. and Y.X.; writing—review and editing, J.W. and J.X.; visualization, J.X.; supervision, T.X.; project administration, J.W.; funding acquisition, J.W., J.C. and J.P. All authors have read and agreed to the published version of the manuscript.

Funding: This research was funded by the Joint Funds of Science Research and Development Program in Henan Province (222103810039, 222103810030), Henan Province Science and Technology key issues (222102220073, 232102111064), and the Key Scientific Research Project of Colleges and Universities in Henan Province (22A460014, 20A460012).

Institutional Review Board Statement: Not applicable.

Informed Consent Statement: Not applicable.

Data Availability Statement: Not applicable.

Conflicts of Interest: The authors declare no conflict of interest.

References

1. Gong, M.; Meng, Y.; Zhang, S.; Zhang, Y.; Zeng, X.; Gao, M. Laser-arc hybrid additive manufacturing of stainless steel with beam oscillation. *Addit. Manuf.* **2020**, *33*, 101180. [CrossRef]
2. Liu, D.; Wu, D.; Wang, R.; Shi, J.; Niu, F.; Ma, G. Formation mechanism of Al-Zn-Mg-Cu alloy fabricated by laser-arc hybrid additive manufacturing: Microstructure evaluation and mechanical properties. *Addit. Manuf.* **2022**, *50*, 102554. [CrossRef]
3. Ma, S.; Jiang, M.; Chen, X.; Li, B.; Jiang, N.; Chen, Y.; Wu, S.; Liang, J.; Li, B.; Lei, Z. Macro/micro-structure and mechanical properties of Al-6Mg-0.3 Sc alloy fabricated by oscillating laser-arc hybrid additive manufacturing. *J. Alloys Compd.* **2022**, *929*, 167325. [CrossRef]
4. Liu, M.; Ma, G.; Liu, D.; Yu, J.; Niu, F.; Wu, D. Microstructure and mechanical properties of aluminum alloy prepared by laser-arc hybrid additive manufacturing. *J. Laser Appl.* **2020**, *32*, 022052. [CrossRef]
5. Zhang, Z.; Sun, C.; Xu, X.; Liu, L. Surface quality and forming characteristics of thin-wall aluminium alloy parts manufactured by laser assisted MIG arc additive manufacturing. *Int. J. Lightweight Mater. Manuf.* **2018**, *1*, 89–95. [CrossRef]
6. Gong, M.; Zhang, S.; Lu, Y.; Wang, D.; Gao, M. Effects of laser power on texture evolution and mechanical properties of laser-arc hybrid additive manufacturing. *Addit. Manuf.* **2021**, *46*, 102201. [CrossRef]
7. Wang, C.; Sun, Y.; Chen, G.; Chen, X.; Ding, J.; Suder, W.; Diao, C.; Williams, S. A simplified modelling approach for thermal behaviour analysis in hybrid plasma arc-laser additive manufacturing. *Int. J. Heat Mass Transf.* **2022**, *195*, 123157. [CrossRef]
8. Garg, A.; Aggarwal, P.; Aggarwal, Y.; Belarbi, M.; Chalak, H.; Tounsi, A.; Gulia, R. Machine learning models for predicting the compressive strength of concrete containing nano silica. *Comput. Concr* **2022**, *30*, 33–42.

9. Garg, A.; Belarbi, M.-O.; Tounsi, A.; Li, L.; Singh, A.; Mukhopadhyay, T. Predicting elemental stiffness matrix of FG nanoplates using Gaussian Process Regression based surrogate model in framework of layerwise model. *Eng. Anal. Bound. Elem.* **2022**, *143*, 779–795. [CrossRef]
10. Meng, L.; McWilliams, B.; Jarosinski, W.; Park, H.-Y.; Jung, Y.-G.; Lee, J.; Zhang, J. Machine learning in additive manufacturing: A review. *Jom* **2020**, *72*, 2363–2377. [CrossRef]
11. Wang, Z.; Jiang, X.; Song, B.; Yang, G.; Liu, W.; Liu, T.; Ni, Z.; Zhang, R. PSO-BP-based morphology prediction method for DED remanufactured deposited layers. *Sustainability* **2023**, *15*, 6437. [CrossRef]
12. Hao, J.; Yang, S.; Le, X.; Królczyk, G.; Sulowicz, M.; Glowacz, A.; Li, Z. Bead morphology prediction of coaxial laser cladding on inclined substrate using machine learning. *J. Manuf. Process.* **2023**, *98*, 159–172. [CrossRef]
13. Wang, K.; Liu, W.; Hong, Y.; Sohan, H.S.; Tong, Y.; Hu, Y.; Zhang, M.; Zhang, J.; Xiang, D.; Fu, H. An overview of technological parameter optimization in the case of laser cladding. *Coatings* **2023**, *13*, 496. [CrossRef]
14. Liu, D.; Liu, C.; Tang, Y.; Gong, C. A GA-BP neural network regression model for predicting soil moisture in slope ecological protection. *Sustainability* **2022**, *14*, 1386. [CrossRef]
15. Inapakurthi, R.K.; Mitra, K. Optimal surrogate building using SVR for an industrial grinding process. *Mater. Manuf. Process.* **2022**, *37*, 1701–1707. [CrossRef]
16. Piri, J.; Abdolahipour, M.; Keshtegar, B. Advanced machine learning model for prediction of drought indices using hybrid SVR-RSM. *Water Resour. Manag.* **2023**, *37*, 683–712. [CrossRef]
17. Zhao, G.; Wang, M.; Liang, W. A comparative study of SSA-BPNN, SSA-ENN, and SSA-SVR models for predicting the thickness of an excavation damaged zone around the roadway in rock. *Mathematics* **2022**, *10*, 1351. [CrossRef]
18. Terrault, N.A.; Hassanein, T.I. Management of the patient with SVR. *J. Hepatol.* **2016**, *65*, S120–S129. [CrossRef]
19. Ramírez-Ochoa, D.-D.; Pérez-Domínguez, L.A.; Martínez-Gómez, E.-A.; Luviano-Cruz, D. PSO, a swarm intelligence-based evolutionary algorithm as a decision-making strategy: A review. *Symmetry* **2022**, *14*, 455. [CrossRef]
20. Huang, J.; Zhou, M.; Zhang, J.; Ren, J.; Vatin, N.I.; Sabri, M.M.S. The use of ga and pso in evaluating the shear strength of steel fiber reinforced concrete beams. *KSCE J. Civ. Eng.* **2022**, *26*, 3918–3931. [CrossRef]
21. Xu, L.; Cao, M.; Song, B. A new approach to smooth path planning of mobile robot based on quartic Bezier transition curve and improved PSO algorithm. *Neurocomputing* **2022**, *473*, 98–106. [CrossRef]
22. Inas, B.; Assam, O.M.; Hamza, B.; Zahia, N. A new PSO-ANN scheme for composite materials properties prediction. In Proceedings of the Online International Symposium on Applied Mathematics and Engineering (ISAME22), Istanbul, Turkey, 21–23 January 2022; p. 36.

Disclaimer/Publisher's Note: The statements, opinions and data contained in all publications are solely those of the individual author(s) and contributor(s) and not of MDPI and/or the editor(s). MDPI and/or the editor(s) disclaim responsibility for any injury to people or property resulting from any ideas, methods, instructions or products referred to in the content.